www.czasopisma.pan.pl PAN POLSKA AKADEMIA NAUK www.journals.pan.pl

Archives of Acoustics Vol. 49, No. 4, pp. 565–574 (2024), doi: 10.24425/aoa.2024.148808

Research Paper

Time-Domain Analysis of Echoes from Solid Spheres and Spherical Shells with Separated Transmit-Receive Configurations

Zhongkai WANG[(1)], Zilong PENG[(1)*], Fulin ZHOU[(2)], Liwen TAN[(1)]

[(1)] *School of Energy and Power*
Jiangsu University of Science and Technology
Zhenjiang, China

[(2)] *State Key Laboratory of Ocean Engineering, Collaborative Innovation Center for Advanced Ship and Deep-Sea Exploration*
Shanghai Jiao Tong University
Shanghai, China

[*]Corresponding Author e-mail: zlp_just@sina.com

(*received February 18, 2024; accepted April 26, 2024; published online August 19, 2024*)

The complexity of bistatic echo pulse sequences surpasses that of monostatic echo pulse sequences. Based on the scattering acoustic field of elastic spheres and spherical shells, a method is employed to calculate the time-domain echoes of solid spheres and spherical shells with transceiver separation under the condition of plane wave incidence. This is achieved by constructing the incident signal and performing a multiplication operation in the frequency domain with the target scattering acoustic field. Employing the contour integral method, we derive phase velocity and group velocity dispersion curves for circumferential waves propagating around these structures. Furthermore, under the assumption of plane wave incidence, we analyze the propagation paths of Rayleigh echoes for solid spheres and anti-symmetric Lamb waves for spherical shells. Estimation formulas for the arrival times of separated transmit-receive echoes are provided for both solid spheres and spherical shells. Our findings indicate that bistatic waves can be classified into clockwise and counterclockwise circulation patterns around the surfaces of these structures. Through a comparison with the time-angle spectrum of echoes, we demonstrate the accuracy of the proposed estimation formulas for echo arrival times. This study offers valuable insights for the identification of underwater targets.

Keywords: dispersion curves; time-domain echoes; bistatic configuration.

1. Introduction

In the context of underwater detection and target identification, when acoustic waves impinge upon the surface of a target, they not only generate geometric reflection waves but also transmit through the target. Within the elastic body, various re-radiated elastic echoes are induced. These echoes carry characteristic information of the target, aiding active sonar systems in the detection and identification of targets (Xia *et al.*, 2016; Too *et al.*, 2014). A considerable amount of research has been conducted globally on the recognition and formation mechanisms of elastic wave components in submerged elastic shell targets, particularly in the domains of ultrasonics, underwater engineering for damage detection (crack detection), and the identification of submerged and seafloor targets (Bednarz, 2017; Apostoloudia *et al.*, 2007; Kargl *et al.*, 2012; Qiao *et al.*, 2016). However, there has been limited research on separated transmit-receive configurations. With the current trend in sonar detection moving towards multi-platform sonar joint detection, the investigation of target identification through the separated transmit-receive configuration, leveraging the scattering characteristics of elastic waves, holds significant importance.

Research on the acoustic scattering of spheres and spherical shells in free fields has been widely conducted both theoretically and experimentally worldwide (Gaunaurd, Werby, 1987; 1991; Ayres *et al.*, 1987; Marston, Sun, 1992). Gaunaurd and Überall (1983; 1985) analyzed the circumferential waves of rigid spheres using singular expansion methods (SEM) and Watson transform techniques, and delved deeper into the scattering processes of solid spheres based on resonance scattering theory. Überall *et al.* (1982) established a direct connection between surface waves and complex frequency poles. Fan *et al.* (2012) applied the Sommerfeld–Watson Transformation (SWT) method to the problem of elastic spherical shells filled with water, employing contour integration to solve dispersion equations in the frequency and wavenumber domains, indicating the generation of a significant amount of fluid-added waves due to internal fluid loading. Ding *et al.* (2023) proposed an acoustic encoding principle and method based on high-frequency time-domain echoes of stratified elastic spherical shells in water, studying the influence of shell thickness, material properties of each layer, and arrangement order on the characteristics of time-domain echoes. Diercks and Hickling (1967) demonstrated through experiments with vacuum spheres that the target echo is related to the receiving point. Anderson (2012) utilized SPWV time-frequency analysis methods and ray theory analysis to show that in the presence of comprehensive effects caused by changes in circumferential wave paths and circumferential wave damping coefficients due to transmit-receive separation, time and frequency shifts occur in the echoes of free-field elastic spherical shells. Thompson (2023) investigated the application of time-frequency methods in detecting and identifying target echoes underwater.

Fawcett (2015) proposed a method for solving the elastic scattering of near-spherical targets, studying the influence of shell thickness on polar angle transformation and showing changes in the mid-frequency enhancement region of near-spherical targets compared to shells with a constant radius. Gunderson *et al.* (2017) obtained forecast formulas for Rayleigh wave interference trajectories of solid spheres and solid cylinders by analyzing the path difference of circumferential waves along their surfaces, both clockwise and counterclockwise, which fit well with the angular frequency spectrum interference fringes of the targets. Yu *et al.* (2014) proposed a subsonic antisymmetric Lamb wave separation method, which can identify subsonic antisymmetric Lamb waves even when the incident short pulse frequency is far from the maximum enhancement frequency. Su *et al.* (2017) proposed a signal processing method under low-frequency broadband long-pulse excitation, allowing the observation and analysis of weak elastic wave energy in strong specular reflection waves. Li and Wu (2019) filtered and modulated target echoes, separating target elastic scattering components. The above studies did not analyze the mechanisms of bistatic echo paths, echo moments, and the information carried by echoes of solid spheres and shells.

This paper firstly establishes a theoretical analytical computational model for solid spheres and spherical shells. By multiplying the spectrum of the constructed sinusoidal pulse signal with the computed acoustic transfer functions of the solid sphere and the spherical shell, the multi-bounce echo spectra of the solid sphere and the spherical shell are obtained. Then, an inverse Fourier transform obtains the time-domain echo pulse sequence. The results reveal that both the bistatic echoes of solid spheres and spherical shells exhibit an X pattern, formed by waves circumnavigating the target in both clockwise and counterclockwise directions. By contrasting the reverse echoes of solid spheres and spherical shells, it is observed that spherical shell reverse echoes exhibit distinct wave packets, which can serve as a reference for the identification of solid spheres and spherical shells. Finally, formulas estimating the arrival times of Rayleigh waves in solid spheres and anti-symmetric waves in spherical shells are provided.

2. Theoretical research

2.1. The theoretical solution of elastic spheres

Harmonic plane sound waves with unit amplitude scatter from the elastic sphere as shown in Fig. 1. Assuming the incident direction is aligned with the z-axis, the backward scattering wave corresponds to $\theta = \pi$. Both the incident and scattered waves are independent of the azimuthal angle φ and symmetric about the z-axis.

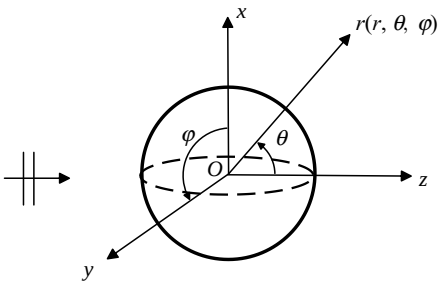

Fig. 1. Plane waves scattering from an elastic sphere.

The expression for the scattered acoustic field of the medium is given by (Tang *et al.*, 2018):

$$p_s = \sum_{n=0}^{\infty} i^n (2n+1) b_n h_n^{(1)}(kr) P_n(\cos\theta), \qquad (1)$$

where θ is the receiving angle, $\mathbf{r}$ is the receiving distance, and $b_n = -B_n/D_n$, with $D_n = 0$ being the characteristic equation of a solid sphere. The terms $h_n^{(1)}(kr)$,

$P_n(\cos\theta)$, and specific elements in the matrix are detailed in (Williams, Marston, 1985).

2.2. The theoretical solution of elastic spherical shells

Scattering of plane waves from a spatially fixed spherical shell is considered, with spherical coordinates r centered at the origin O, where the outer radius of the shell is a, the inner radius is b, the thickness is $h = a - b$, and the interior of the shell is a vacuum (Fig. 2). Assume a unit amplitude harmonic plane wave incident along the z-direction onto the spherical shell.

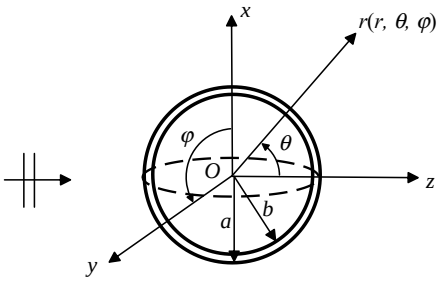

Fig. 2. Schematic diagram of elastic spherical shell scattering.

The boundary conditions of the spherical shell are:

$$\begin{cases} T_{rr} = -p, \\ u_r = \dfrac{1}{\rho_0 w^2}\dfrac{\partial p}{\partial r}, \\ T_{r\theta} = 0, \end{cases} \qquad r = a, \tag{2}$$

$$\begin{cases} T_{rr} = 0, \\ T_{r\theta} = 0, \end{cases} \qquad r = b, \tag{3}$$

where T_{rr} and $T_{r\theta}$ represent stress, and u_r represents displacement.

To solve for the scattering coefficient B_n from the boundary conditions, we use the expression $b_n = -B_n/D_n$, where $D_n = 0$ is the characteristic equation of the spherical shell, and the matrix elements B_n and D_n can be found in (Gaunaurd, Werby, 1991). The scattered acoustic pressure in the surrounding water medium of the spherical shell can still be expressed using Eq. (1).

3. Algorithm verification

To ascertain the precision of the computational modeling of the scattering acoustic fields associated with elastic spheres and spherical shells, we conducted separate calculations for the scattering acoustic fields of a copper sphere with a radius of 0.5 m and a vacuum copper shell with equivalent dimensions and a thickness-to-diameter ratio of 0.05 (Fig. 3). The material properties are detailed in Table 1. The outcomes generated by the algorithm proposed in this study were juxtaposed with those derived from finite element software tailored for two-dimensional axisymmetric computations. The comparative findings are depicted in Fig. 4. It is evident from the results that the two computational approaches exhibit a high degree of agreement, thus affirming the accuracy of the proposed methodology.

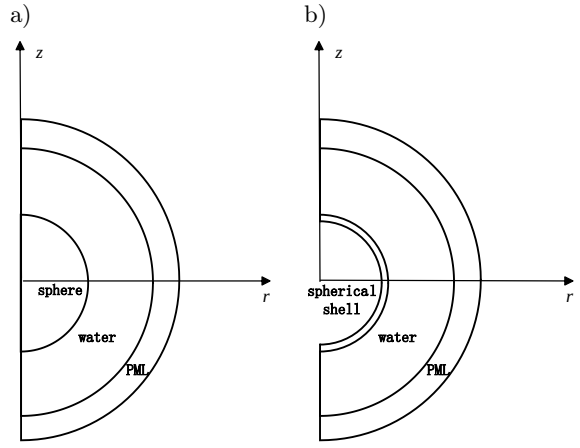

Fig. 3. Finite element software two-dimensional axisymmetric acoustic scattering model: a) sphere; b) spherical shell.

Table 1. Material parameters.

Material	Density [kg/m^3]	Longitudinal wave speed (c_l) [m/s]	Transverse wave speed (c_t) [m/s]
Water	1000	1500	–
Copper	8900	4759	2325

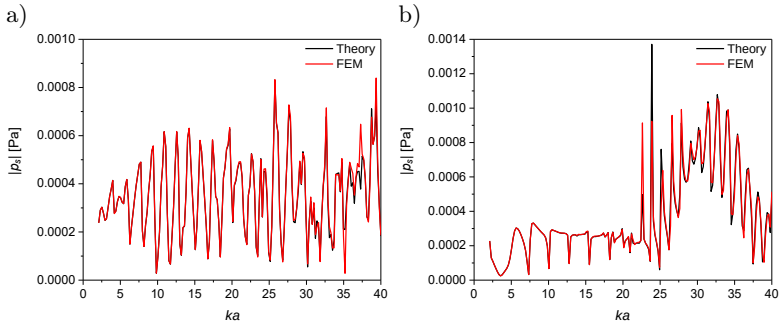

Fig. 4. Comparison of theoretical solution and finite element computational results (ka is dimensionless frequency): a) sphere; b) spherical shell.

4. Dispersion curve

4.1. Solid sphere dispersion curve

The object of study in this section is a copper sphere with a radius of 0.06 m. Utilizing both contour integration and Gaussian integration methods (Long *et al.*, 1994), we computationally determine the phase velocity and group velocity dispersion curves for the elastic copper sphere with a radius of 0.06 m. The material parameters used for these calculations are outlined in Table 1. The resulting dispersion curves are visually represented in the subsequent figure (Fig. 5). It is evident that the principal types of circumferential waves in the elastic sphere include whispering gallery (W-G) waves, Rayleigh waves, and Franz waves. A higher imaginary component of the root signifies a more pronounced radiation capability; however, it also corresponds to increased attenuation during propagation (Tang *et al.*, 2018). Notably, the imaginary component of Franz waves surpasses that of Rayleigh waves, indicating that Franz waves experience heightened attenuation compared to Rayleigh waves (Fig. 6). Consequently, the observation of Franz waves in backward scattering scenarios poses considerable difficulty.

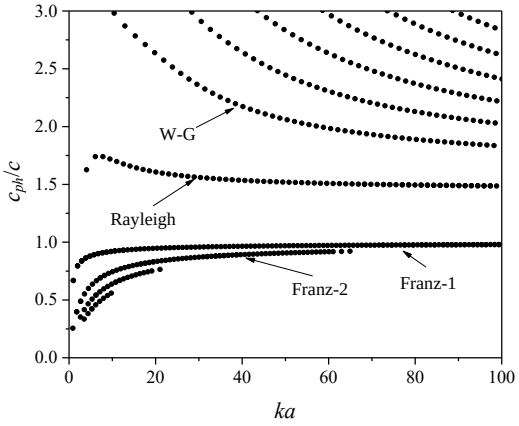

Fig. 5. Phase velocities.

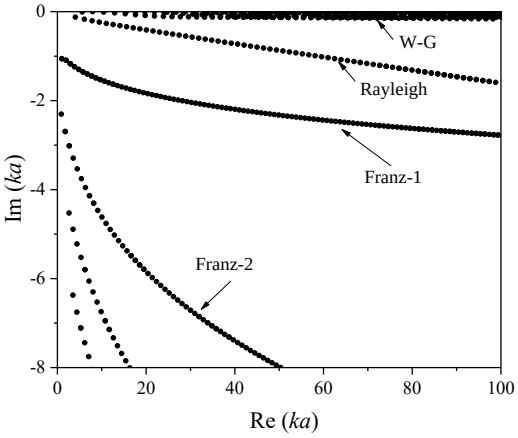

Fig. 6. Distribution plot of the real and imaginary parts.

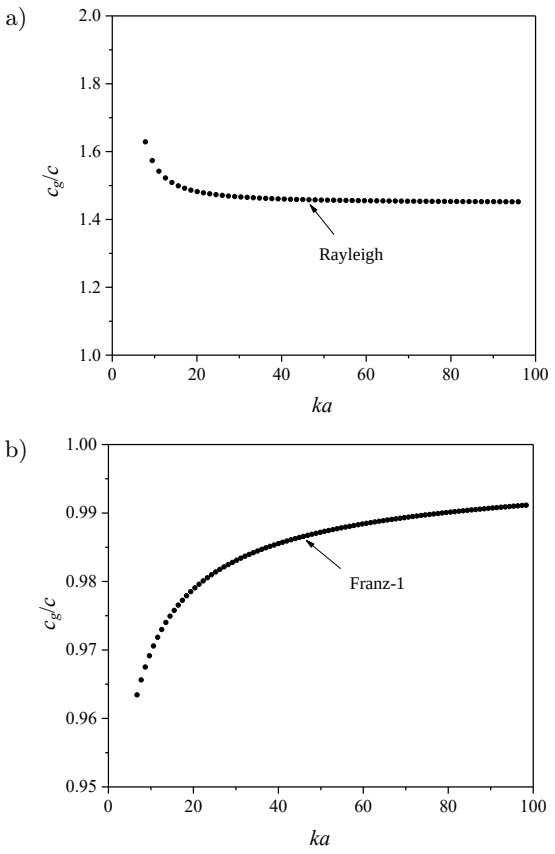

Fig. 7. Group velocities: a) Rayleigh; b) Franz-1.

4.2. Spherical shell dispersion curve

Similar to solving the dispersion curve of a solid sphere, all that is required is to modify the characteristic equation of the sphere to that of a spherical shell. The dispersion curve of the phase velocity for a vacuum copper spherical shell with a radius of 0.06 m and a thickness-to-radius ratio of 0.05 is depicted in Fig. 8. It can be observed that the a_{0+} and a_{0-} waves undergo a bifurcation near the resonance frequency.

From Fig. 9, it is evident that the imaginary component of the a_{0-} wave is nearly negligible at low fre-

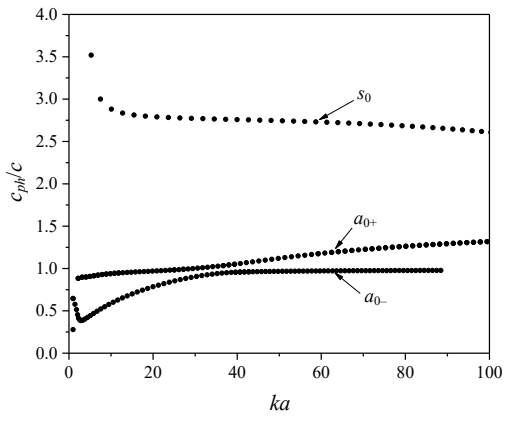

Fig. 8. Phase velocity dispersion curves.

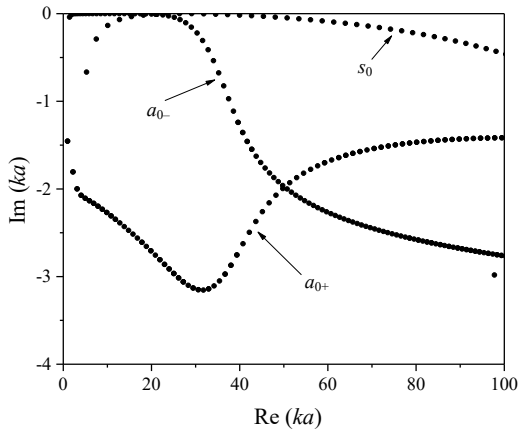

Fig. 9. Distribution plot of the real and imaginary parts.

quencies, suggesting a low radiation efficiency for this wave type within this frequency range. Consequently, the detection of the a_{0-} wave at low frequencies proves challenging. Moreover, a discernible trend is observed wherein the radiation efficiency of the a_{0-} wave increases from low to high frequencies, while conversely, the radiation efficiency of the a_{0+} wave decreases from high to low frequencies, with a notable inflection point near the resonance frequency. Notably, the imaginary component of the s_0 wave remains consistently minimal near the resonance frequency, indicating relatively weak radiation characteristics for this wave type. The calculated group velocity curve of the a_{0-} wave is shown in Fig. 10.

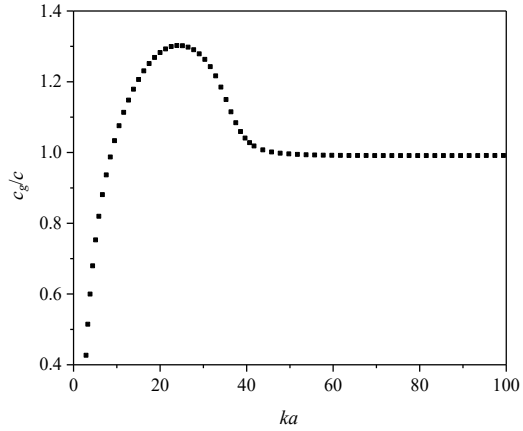

Fig. 10. Group velocities of the a_{0-} wave.

5. Time-domain analysis

The time domain echo calculation of the target mainly includes: constructing the sinusoidal signal as the incident wave, and using the fast Fourier transform to get the incident wave spectrum. The scattering sound pressure of the target is obtained as the transfer function by theoretical solution. The frequency spectrum of the incident signal and the transfer function are multiplied in the frequency domain, and the echo pulse sequence of the target is obtained by inverse Fourier transform.

5.1. Sphere

A single-cycle 120 kHz ($ka \approx 30$) sine wave is used as the incident signal. At this point, the phase velocity is approximately 2325 m/s, and the group velocity is approximately 2194 m/s. According to the law of refraction:

$$\sin(\theta_c) = c/c_{ph}, \tag{4}$$

where c is the speed of sound in water, which is 1500 m/s. The critical angle θ_c is approximately 40°. This means that the incident wave enters the surface at the critical angle of 40° and radiates outward at the critical angle.

5.1.1. Monostatic configuration

For the backward wave, taking clockwise as an example, the path of the circumferential wave is shown in Fig. 11. The incident wave couples into the spherical surface at point A, decouples and propagates outward at point B. Afterward, a portion of the circumferential wave continues to circulate around the spherical surface for one revolution before decoupling from point B, and so on.

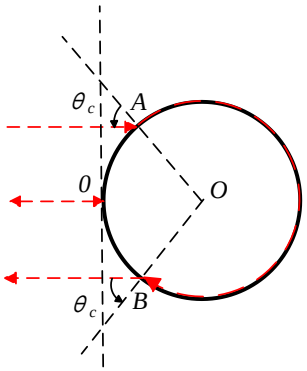

Fig. 11. Propagation path (clockwise).

In order to achieve a more succinct echo curve, a matched filtering technique is applied, utilizing the constructed incident signal as the reference signal. The resulting time-domain echo is matched filtered, yielding the echo curve as shown in Fig. 12. Using the mirror reflection echo at the top 0 as the time reference point, the propagation time between $R1$ and $R2$ is determined to be the time it takes for the wave to complete one full circulation around the spherical surface. This enables the calculation of the Rayleigh wave group velocity, which is approximately 2194 m/s. This value aligns with the Rayleigh wave velocity calculated in the previous section.

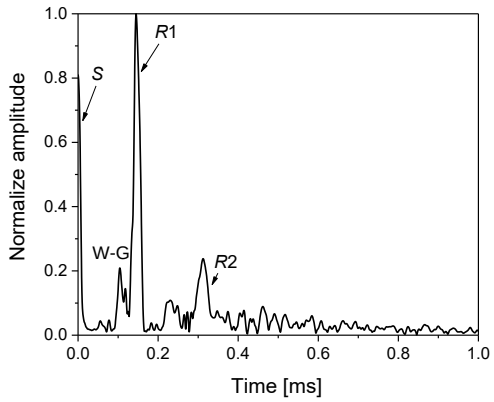

Fig. 12. Impulse responses.

5.1.2. Bistatic configuration

The time-domain echo of a separated transmit-receive elastic sphere is computed, with the foremost bright line representing the specular echo. The position of this bright line changes with variations in the receiving angle. Upon further observation, it is noted that the time-domain echo pattern of the elastic sphere with a separated transmit-receive configuration exhibits an X-mode, which is attributed to the influence of the circumferential components of Rayleigh waves. Rayleigh waves propagate along the surface of the solid sphere in both clockwise (CW) and counterclockwise (CCW) directions. The sphere possesses a strictly symmetric structure, and the waves circumnavigate the sphere's surface, eventually superimposing in the opposite direction of the shell (θ = 180°). Consequently, bright spots are observed at the 180° angle in Fig. 13b.

According to the propagation paths of the waves, they can be divided into clockwise circumferential propagation around the sphere and counterclockwise circumferential propagation around the sphere, as shown in Figs. 14 and 15.

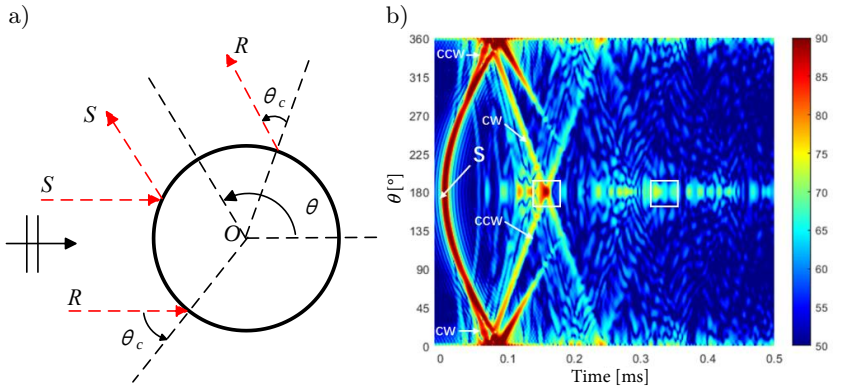

Fig. 13. a) Schematic for the acoustic scattering problem under consideration; b) the bistatic impulse response of the sphere.

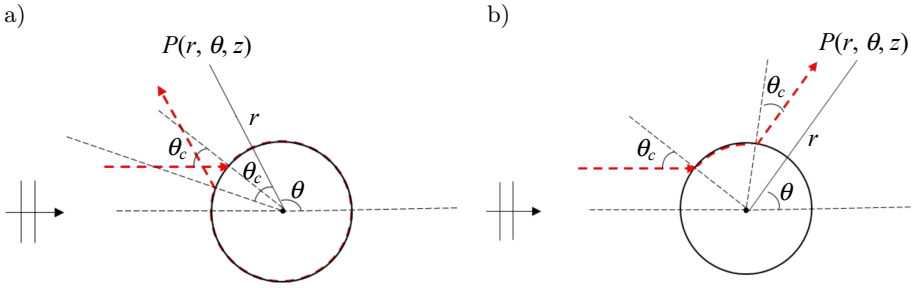

Fig. 14. Propagation path (CW): a) $\pi - \theta < 2\theta_c$; b) $\pi - \theta > 2\theta_c$.

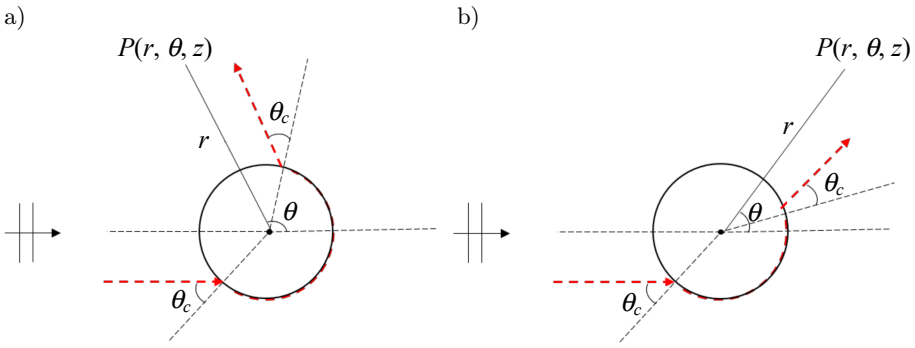

Fig. 15. Propagation path (CCW): a) path 1; b) path 2.

The formula for estimating the arrival time of the echo is given as follows, where $\theta = \pi$ corresponds to the moment of arrival of the reverse echo:

$$t_{\mathrm{CCW}} = \frac{2a(1-\cos(\theta_c))}{c} + \frac{a(\pi+\theta-2\theta_c)}{c_R^g} + (n-1)\frac{2\pi a}{c_R^g}, \tag{5}$$

$$t_{\mathrm{CW}} = \begin{cases} \dfrac{2a(1-\cos(\theta_c))}{c} + \dfrac{a(\pi-\theta-2\theta_c)}{c_R^g} + (n-1)\dfrac{2\pi a}{c_R^g}, & \pi-\theta > 2\theta_c, \\ \dfrac{2a(1-\cos(\theta_c))}{c} + \dfrac{a(3\pi-\theta-2\theta_c)}{c_R^g} + (n-1)\dfrac{2\pi a}{c_R^g}, & \text{else.} \end{cases} \tag{6}$$

The sphere is a strictly symmetrical structure, so the characteristics of echoes between angles 0°~180° and angles 180°~360° are consistent. This article uses the range of 0°~180° as an example. Based on the formula mentioned earlier to determine the echo arrival time, it can be observed that the curves correspond well with the echo fringes. The relationship between the mirrored echo angle and the echo arrival time follows a sine function, causing the echo fringes to be curved. The first echo of Rayleigh waves has a slope of c_R^g/a, which is positively correlated with the velocity of Rayleigh waves, making the fringe a straight line. At angles below approximately 100°, clockwise echoes reach the receiving point earlier than geometric echoes. Besides the Rayleigh wave echoes (labeled as 1 in Fig. 16), other echoes are observed, possibly corresponding to a combination of W-G waves and other transmitted waves (Williams, Marston, 1985). It can also be observed that as the angle approaches the forward direction, a segment of echoes is observed (labeled as 2 in Fig. 16). It is challenging to observe this segment of echoes near the reverse angle. By calculating the arrival time of echoes using the subsonic Franz-1 wave velocity (Fig. 7b), it is observed that this segment of echoes corresponds well with the echo fringes. Therefore, these echoes may be associated with subsonic waves.

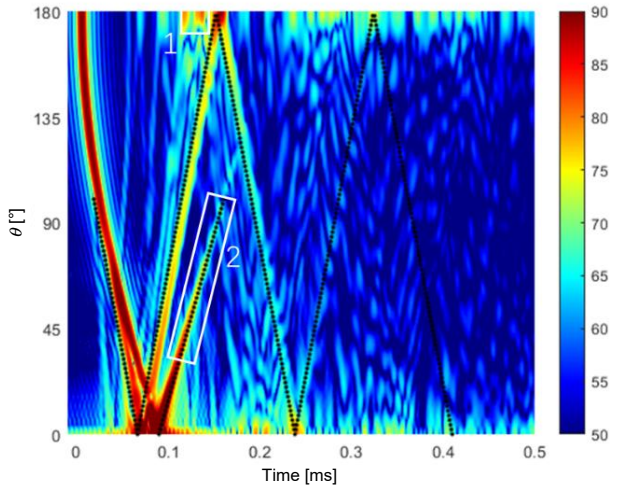

Fig. 16. Bistatic impulse response of the sphere.

5.2. Spherical shell

Calculating the form function of a vacuum copper spherical shell with a radius of 0.06 m and a thickness-to-diameter ratio of 0.05, it can be observed that the elastic shell exhibits a noticeable mid-frequency enhancement ($ka \approx 18$~42).

When using a single-cycle 120 kHz ($ka \approx 30$) sine signal as the incident signal, and referring to the dispersion curve calculated in Fig. 17, it can be observed that around the resonance frequency, the bending wave on the surface of the spherical shell in water corresponds to the a_{0-} wave. This indicates indicating that the incident acoustic wave enters tangentially ($\theta_c \approx \pi/2$) along the surface of the spherical shell and leaks into the water at an angle of θ_c.

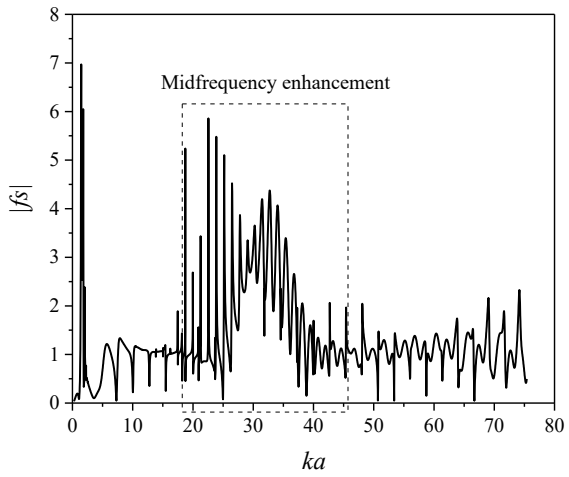

Fig. 17. Form function of a vacuum copper spherical shell.

5.2.1. Monostatic configuration

The incident wave enters tangentially onto the surface of the spherical shell, and the paths of clockwise and counterclockwise propagation of the circumferential waves are illustrated in Fig. 18. The incident wave couples into the sphere at points $A(A')$, decouples and propagates outward at points $B(B')$. Some of the circumferential waves continue to propagate along the surface of the shell for one complete revolution before decoupling and radiating outward from points $B(B')$. This process repeats, resulting in a sequence of echo pulses.

Due to the narrow pulse during signal emission, the propagation velocity needs to be determined using

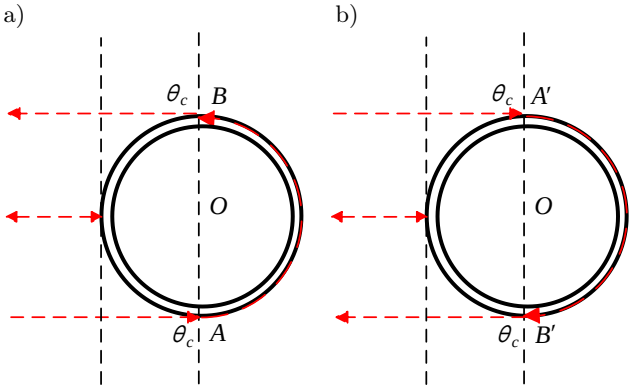

Fig. 18. Propagation path ($\theta_c \approx \pi/2$): a) CCW; b) CW.

the group velocity (Tang *et al.*, 2018). Calculations yield an approximate group velocity of about 1900 m/s for the a_{0-} wave. Using the estimated arrival time Eq. (9) based on the time when the echo arrives, with the echo reflected from the retroreflector as the time reference point, the calculated times are plotted against the time-domain echo curve. Three plotted curves from left to right (Fig. 19) represent the first, second, and third antisymmetric echoes. It can be observed that the calculated echo arrival times correspond well with the time-domain curves.

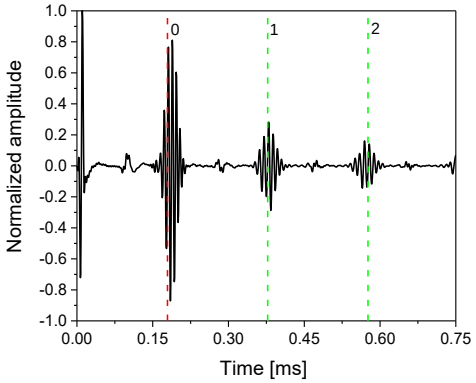

Fig. 19. Impulse responses.

5.2.2. Bistatic configuration

The time-domain echoes of the elastic spherical shell in the separate transmit-receive configuration were calculated. Upon observation, similarities were found with the characteristics of the bistatic echoes from the copper sphere. At the forefront, there is a bright line corresponding to the mirror image echo, and the position of this line changes with variations in the receiving angle. The time-domain echo pattern in the separate transmit-receive configuration for the elastic spherical shell resembles an X-mode, influenced by the circumferential components of the a_{0-} wave (Anderson, 2012). The a_{0-} wave propagates clockwise and counterclockwise along the surface of the spherical shell. Due to the strict symmetry of the shell structure, the paths of waves propagating clockwise and counterclockwise along the surface are identical. Consequently, they intersect in the opposite direction of the shell ($\theta = 180°$), resulting in a bright spot at 180° in the graph, which is the culmination of the superposition of circumferential waves (Fig. 20).

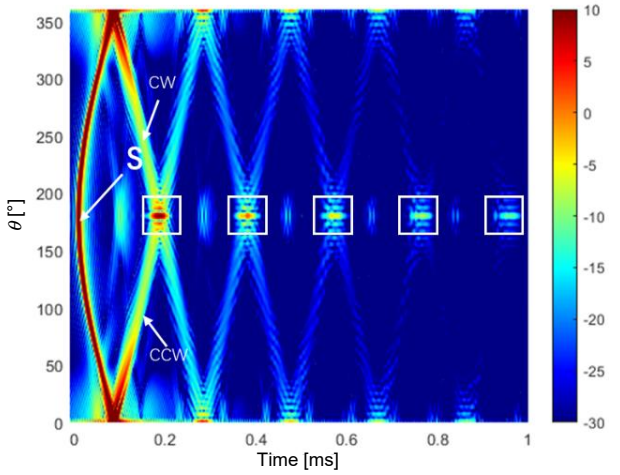

Fig. 20. Bistatic impulse response of the spherical shell.

According to the preceding section, the incident wave enters tangentially onto the surface of the spherical shell. When propagating counterclockwise, the incident acoustic wave couples from point A to point B and decouples to radiate outward. The angle corresponding to the circumferential wave path on the shell surface is θ_1. When propagating clockwise, the incident acoustic wave couples from point A' to point B' and decouples to radiate outward. The angle corresponding to the circumferential wave path on the shell surface is θ_2.

Observe the above diagram (Fig. 21) to obtain the angles corresponding to counterclockwise and clockwise circumferential waves:

$$\theta_1 = \theta, \tag{7}$$

$$\theta_2 = 2\pi - \theta. \tag{8}$$

Calculate the arrival times of counterclockwise and clockwise circumferential waves along the surface of the spherical shell based on the propagation paths:

$$t_{\mathrm{CCW}} = \frac{2a}{c} + a\frac{\theta_1}{c^g_{a_{0-}}} + (n-1)\frac{2\pi a}{c^g_{a_{0-}}}, \tag{9}$$

$$t_{\mathrm{CW}} = \frac{2a}{c} + a\frac{\theta_2}{c^g_{a_{0-}}} + (n-1)\frac{2\pi a}{c^g_{a_{0-}}}. \tag{10}$$

The time difference between the arrivals of counterclockwise and clockwise circumferential waves is given by Eq. (11). It can be observed that when the backward echo occurs $\theta = \pi$, the time difference between clockwise and counterclockwise waves is 0:

$$\Delta_t = t_{\mathrm{CW}} - t_{\mathrm{CWW}} = a\frac{\theta_2 - \theta_1}{c^g_{a_{0-}}} = a\frac{2(\pi - \theta)}{c^g_{a_{0-}}}. \tag{11}$$

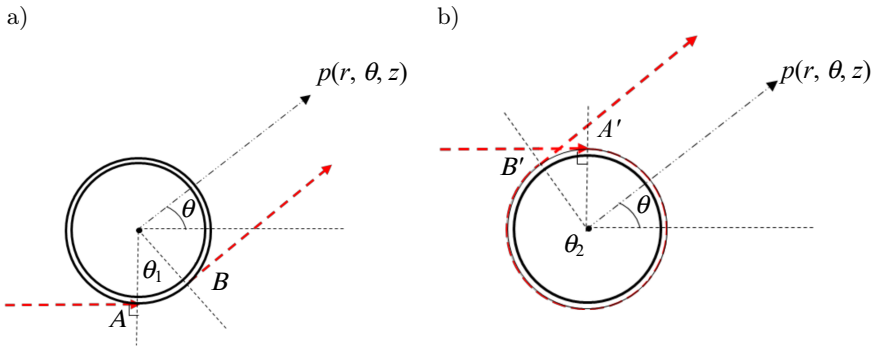

Fig. 21. Propagation path: a) CCW; b) CW.

When the circumferential wave reaches point B or B', a portion decouples and radiates outward, while another portion continues to circumnavigate the spherical shell before decoupling and radiating outward. The remaining part continues to circumnavigate along the surface of the spherical shell. Therefore, the time difference between adjacent echoes of clockwise or counterclockwise echoes is the time it takes for the circumferential wave to complete one full rotation along the surface of the spherical shell:

$$\Delta_{t0} = \frac{2\pi a}{c^g_{a_{0-}}}. \tag{12}$$

According to the formula for estimating the echo timing, the bistatic echoes are calculated and plotted on the time-angle spectrum. Since the spherical shell is a strictly symmetric structure, this paper takes the example of 0°~180°. It can be observed that the calculated echo timings correspond well with the time-angle spectrum (Fig. 22).

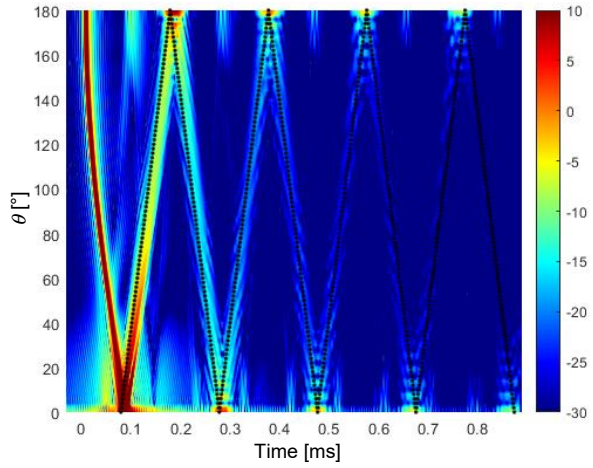

Fig. 22. Bistatic impulse response of the spherical shell.

6. Conclusions and discussion

This research computed the time-domain echoes of solid spheres and spherical shells under plane wave incidence by employing a method that constructs the incident signal and performs multiplication operations in the frequency domain with the target scattering acoustic field. Based on the scattering acoustic field of elastic spheres and spherical shells, the following main conclusions are drawn:

1) Under the same planar wave incident signal, echoes from solid spheres are more complex compared to those from spherical shells. At specific frequencies, solid spheres predominantly exhibit Rayleigh and W-G waves, while spherical shells mainly manifest a_{0-} waves, with a noticeable mid-frequency enhancement phenomenon. In the time-domain echoes, this is evident as distinct wave packets, offering valuable insights for distinguishing between solid spheres and spherical shells underwater.
2) The study reveals that, for elastic spheres within the near-forward angle range, elastic waves arrive faster than specular echoes. This phenomenon is attributed to the azimuthal function of the circumferential wave arrival time on the spherical surface, which is dependent on the circumferential wave velocity and path.
3) By examining the relationship between echo arrival time and reception angle, it is observed that a small segment of the echo can be observed near the forward angle, whereas this segment of the echo is not observed near the backward angle. Computational analysis reveals that this segment of the echo corresponds to subsonic waves.
4) The echo arrival times of separated transmit-receive configurations for elastic spheres and spherical shells can be predicted. Estimation formulas for the bistatic echo arrival times of the two targets are provided, showing good agreement between the predicted echo arrival times and the time-domain echo curves.

Acknowledgments

This study was supported by the National Natural Science Youth Fund (52201397) and the Jiangsu Graduate Practical Innovation Program (SJCX23_2215).

References

1. Anderson S.D. (2012), *Space-time-frequency processing from the analysis of bistatic scattering for simple underwater targets*, Ph.D. Thesis, College of Engineering, George W. Woodruff School of Mechanical Engineering.
2. Apostoloudia A., Douka E., Hadjileontiadis L.J., Rekanos I.T., Trochidis A. (2007), Crack detection on beams by time-frequency analysis of transient flexural waves, *Archives of Acoustics*, **32**(4): 941–954.
3. Ayres V.M., Gaunaurd G.C., Tsui C.Y., Werby M.F. (1987), The effects of Lamb waves on the sonar cross-sections of elastic spherical shells, *International Journal of Solids and Structures*, **23**(7): 937–946, doi: 10.1016/0020-7683(87)90088-6.
4. Bednarz J. (2017), Operational modal analysis for crack detection in rotating blades, *Archives of Acoustics*, **42**(1): 105–112, doi: 10.1515/aoa-2017-0011.
5. Diercks K.J., Hickling R. (1967), Echoes from hollow aluminum spheres in water, *The Journal of the Acoustical Society of America*, **41**(2): 380–393, doi: 10.1121/1.1910349.
6. Ding D., Chen C.X., Kong H.M., Fan J., Peng Z.L. (2023), Acoustic coding based on high frequency time domain echo of layered elastic spherical shells in water [in Chinese], *Applied Acoustics*, **42**(4): 781–791.
7. Fan W., Fan J., Wang X.N. (2012), Application of the SWT method to scattering from water-filled elastic spherical shells [in Chinese], *Journal of Ship Mechanics*, **16**(6): 705–715.
8. Fawcett J.A. (2015), Computing the scattering from slightly deformed spherical shells, *IEEE Journal of Oceanic Engineering*, **41**(3): 682–688, doi: 10.1109/JOE.2015.2478995.
9. Gaunaurd G., Überall H. (1985), Relation between creeping-wave acoustic transients and the complex-frequency poles of the singularity expansion method, *The Journal of the Acoustical Society of America*, **78**(1): 234–243, doi: 10.1121/1.392564.
10. Gaunaurd G.C., Überall H. (1983), RST analysis of monostatic and bistatic acoustic echoes from an elastic sphere, *The Journal of the Acoustical Society of America*, **73**(1): 1–12, doi: 10.1121/1.388839.
11. Gaunaurd G.C., Werby M.F. (1987), Lamb and creeping waves around submerged spherical shells resonantly excited by sound scattering, *The Journal of the Acoustical Society of America*, **82**(6): 2021–2033, doi: 10.1121/1.395646.
12. Gaunaurd G.C., Werby M.F. (1991), Sound scattering by resonantly excited, fluid-loaded, elastic spherical shells, *The Journal of the Acoustical Society of America*, **90**(5): 2536–2550, doi: 10.1121/1.402059.
13. Gunderson A.M., España A.L., Marston P.L. (2017), Spectral analysis of bistatic scattering from underwater elastic cylinders and spheres, *The Journal of the Acoustical Society of America*, **142**(1): 110–115, doi: 10.1121/1.4990690.
14. Kargl S.G., Williams K.L., Thorsos E.I. (2012), Synthetic aperture sonar imaging of simple finite targets, IEEE *Journal of Oceanic Engineering*, **37**(3): 516–532, doi: 10.1109/JOE.2012.2200815.
15. Li X., Wu Y. (2019), Feature extraction for acoustic scattering from a buried target, *Journal of Marine Science and Application*, **18**: 380–386, doi: 10.1007/s11804-019-00102-9.
16. Long Y.L., Wen X.L., Xie C.F. (1994), An implementation of a root finding algorithm for transcendental functions in a complex plane [in Chinese], *Journal on Numerical Methods and Computer Applications*, pp. 88–92.
17. Marston P.L., Sun N.H. (1992), Resonance and interference scattering near the coincidence frequency of a thin spherical shell: An approximate ray synthesis, *The Journal of the Acoustical Society of America*, **92**(6): 3315–3319, doi: 10.1121/1.404181.
18. Qiao S., Shang X., Pan E. (2016), Elastic guided waves in a coated spherical shell, *Nondestructive Testing and Evaluation*, **31**(2): 165–190, doi: 10.1080/10589759.2015.1079631.
19. Su J., Wang F., Du S. (2017), An elastic wave enhancement method based on modified bright point model, [in:] *2017 IEEE International Conference on Signal Processing, Communications and Computing* (*ICSPCC*), pp. 1–4, doi: 10.1109/ICSPCC.2017.8242491.
20. Tang W.L., Fan J., Ma Z.C. (2018), Elastic acoustic scattering mechanism of targets in water, *The Acoustic Scattering of Underwater Target* [in Chinese], pp. 79–84, Science Press, China.
21. Thompson M. (2023), *Time-frequency sonar detection of elastic wave reradiation*, Ph.D. Thesis, Electrical and Computer Engineering, Auburn Universit.
22. Too G.P., Lin Y.W., Ke Y.C. (2014), Echoes analysis from spherical elastic shells by using iterative time reversal mirror, [in:] *OCEANS 2014 – TAIPEI*, pp. 1–5, doi: 10.1109/OCEANS-TAIPEI.2014.6964463.
23. Überall H., Gaunaurd G.C., Murphy J.D. (1982), Acoustic surface wave pulses and the ringing of resonances, *The Journal of the Acoustical Society of America*, **72**(3): 1014–1017, doi: 10.1121/1.388232.
24. Williams K.L., Marston P.L. (1985), Backscattering from an elastic sphere: Sommerfeld–Watson transformation and experimental confirmation, *The Journal of the Acoustical Society of America*, **78**(3): 1093–1102, doi: 10.1121/1.393028.
25. Xia Z., Li X., Meng X. (2016), High resolution time-delay estimation of underwater target geometric scattering, *Applied Acoustics*, **114**: 111–117, doi: 10.1016/j.apacoust.2016.07.016.
26. Yu X., Peng L., Yu G. (2014), Extracting the subsonic anti-symmetric lamb wave from a submerged thin spherical shell backscattering through iterative time reversal, *Journal of Ocean University of China*, **13**: 589–596, doi: 10.1007/s11802-014-2166-8.